

Mn(II)-doped 2D perovskite for light emitting devices

Daniele Cortecchia, Wojciech Mróz, Stefanie Neutzner, Tetiana Borzda, Giulia Folpini, Annamaria Petrozza*

Istituto Italiano di Tecnologia, Milan, 20133, Italy

**Corresponding Author: Annamaria.Petrozza@iit.it*

SUMMARY

Low dimensional perovskites are considered good candidates for light emitting applications given the high exciton binding energy which should in principle improve the radiative recombination efficiency. Yet, single-layered two-dimensional (2D) perovskite films are strongly limited by trap-assisted recombination and suffer from low luminescence yields, hampering their application in electroluminescence devices. Here, we use *ad hoc* synthetic and defect engineering strategies to overcome such issue. We employ metallic doping to controllably introduce luminescent impurities in a matrix made of 2D perovskite NMA_2PbX_4 based on the cation $\text{NMA} = 1\text{-naphtylmethylammonium}$. By means of temperature-dependent and time-resolved spectroscopy we demonstrate efficient energy transfer to Mn^{2+} centres. Such process avoids the funnelling of the photo-excited species in inefficient recombination channels represented by intra-gap trap states and enhances photoluminescence, with quantum yield surpassing 20% in doped films. Eventually, we embody Mn-doped $\text{NMA}_2\text{PbBr}_4$ in a light emitting diode architecture and show, for the first time, electroluminescence from the $\text{Mn}^{2+}:^4\text{T}_1 \rightarrow ^6\text{A}_1$ transition. This proof-of-concept demonstration shows the potential of doping in layered perovskites and prompt for the study of a wider range of host/guest structures.

INTRODUCTION

In the last years, metal halide perovskites have been attracting increasing interest for light emitting applications such as light-emitting diodes (LEDs) and field-effect transistors (FETs), lasing and scintillators.¹⁻⁷ Three-dimensional (3D) perovskites have emerged as the best candidate for high-efficiency solar cells,⁸ and they have been demonstrated recently also in efficient LEDs.⁹⁻¹¹ Nevertheless, the research community keeps exploring alternative structures to improve the efficiency of radiative recombination.^{12,13} The possibility to sensibly increase the exciton binding energy (up to few hundreds meV) by exploiting spatial and dielectric confinement in low-dimensional structures formed by the alternation of organic and inorganic sheets has revived the interest in two-dimensional (2D) perovskites.^{14,15} Impressive results have been achieved with multidimensional Ruddlesden-Popper perovskites, where the creation of perovskite films with self-organized heterogeneous phases is exploited to realize a cascade energy transfer from 2D perovskites with large band gap to 3D perovskite domains with narrower band gap, achieving photoluminescence quantum yield (PLQY) values up to 60% and external quantum efficiencies (EQE) beyond 14% in LEDs.¹⁶⁻²² However, with the exception of photoluminescence measured on exfoliated perovskite single crystals,²³ most of the single-layered 2D perovskites reported so far suffer from very low PLQY <3% when processed in form of thin films, which have frustrated the fabrication of efficient LEDs and their room temperature operability.^{20,24-30} Although the origin of the inefficient

radiative recombination in these single-layered 2D structures is not yet fully understood, it is likely to stem from fast exciton quenching at room temperature and their high trap density,³¹⁻³³ which is consistent with the observation of ultrabroadband largely Stokes shifted luminescence in several compounds of this family.^{24,34} Careful synthetic design and defect engineering might represent the key to avoid rapid non-radiative quenching and improve the luminescence yield and tunability of 2D perovskites. Two strategies can be identified, involving the use of photoactive organic cations or the addition of selected heteroatoms to the perovskite lattice. In the first case, energy transfer to functional templating cations (such as quaterthiophene derivatives) has been exploited to improve the light emitting properties of layered perovskites, in some cases with successful integration in electroluminescent devices.³⁵⁻³⁷ On the other hand, doping with transition metals (Mn^{2+}) and rare earth metals (especially Yb^{3+} and Ce^{3+}) have been recently investigated in 3D perovskites nanocrystals such as $\text{CsPbBr}_x\text{Cl}_{3-x}$, where the luminescence from the energy levels of the dopant led to a substantial PLQY enhancement.³⁸⁻⁴⁹ For example, PLQYs of Mn-doped CsPbCl_3 nanocrystals typically reaches 30-40%;⁵⁰ however, such high efficiencies are usually reported in colloidal dispersions, while it is challenging to preserve them in solid-state, due to the severe luminescence quenching encountered in CsPbCl_3 nanocrystals when deposited as thin films.^{23,51} Thanks to the wider band gap compared to their 3D homologues, 2D perovskites can serve as excellent host materials to achieve efficient energy transfer to guests dopants. Among 2D perovskites, successful doping with PL enhancement comparable to 3D perovskite nanocrystals has been reported only in BA_2PbBr_4 (BA=butylammonium),⁵² however the mechanisms underlying the luminescence enhancement of these systems are yet to be clarified. Moreover, to date, there are no reports about their actual integration in electroluminescent devices.

In this work, we investigate the use of a photoactive organic cation and an inorganic dopant to overcome the fast exciton quenching in single-layered 2D perovskites by using $(\text{NMA})_2\text{PbX}_4$ (where NMA = 1-naphthylmethylammonium) as a host matrix for manganese doping. NMA is a molecule with energy of the triplet state comparable to the Mn^{2+} : ${}^4\text{T}_1 \rightarrow {}^6\text{A}_1$ transition characteristic of the inorganic dopant, and are both ideally placed to allow an active role in the luminescent properties of the material.⁵³⁻⁵⁶ By means of temperature dependent and time-resolved spectroscopy, we show that energy transfer from the perovskite's PbBr_4^{2-} inorganic layers can occur to both the NMA cation and the Mn^{2+} guest ions with consequent spectral tuning of the perovskite emission. However, only in the case of metallic doping highly efficient energy transfer is achieved, allowing to overcome the exciton trapping process and leading to luminescent enhancement with $\text{PLQY} > 20\%$ in spin-coated bulk films. To test the effectiveness of the doping strategy for light-emitting devices, for the first time we employed Mn^{2+} -doped $\text{NMA}_2\text{PbBr}_4$ as an active material achieving orange electroluminescence in LEDs operable at room temperature. This proof-of-concept demonstration paves the way to new synthetic strategies for improving the luminescence properties and spectral tunability of low-dimensional perovskites.

RESULTS AND DISCUSSIONS

Films of $\text{NMA}_2\text{PbBr}_4$ were spin-coated from DMF solutions by dissolving the organic salt (NMA)Br and the inorganic precursor PbBr_2 in 2:1 stoichiometric ratio, while for the doped material MnBr_2 was added to the spin coating solution. Doped samples are indicated here with the notation $\text{NMA}_2\text{PbBr}_4:\text{Mn}(x)$, where x indicates the molar ratio of manganese with respect to lead in the starting solution. The formation of the perovskite $\text{NMA}_2\text{PbBr}_4$ was confirmed by X-ray diffraction performed on both powders and thin films (Fig. 1A and S1): as typically observed with such 2D perovskites, in the case of the spin-coated film only some of the diffraction peaks are visible (4.73° , 9.37° , 14.05°) due to the strong preferential orientation of the perovskite on the substrate (Fig. 1A). To study the effects of Mn inclusion on the perovskite structure, we investigated $\text{NMA}_2\text{PbBr}_4:\text{Mn}(x)$ over the compositional range $x=0\text{-}30\%$ mol (Fig. 1A). Upon manganese addition, the host structure is perfectly retained and the absence of additional diffraction peaks excludes the phase segregation of a Mn-based perovskite (for example $\text{NMA}_2\text{MnBr}_4$, Fig. 1A). A gradual change in the relative intensities of the host diffraction peaks is observed, which can be due either to a change in the scattering factors after doping or to a slight difference in the preferential orientation induced by the presence of Mn. Previous works have demonstrated that manganese doping in 3D lead perovskite nanocrystals proceeds with partial substitution of the octahedrally coordinated Pb^{2+} with the isovalent ion Mn^{2+} . Given the bigger ionic size of Pb^{2+} (133 pm) compared to Mn^{2+} (81 pm) lattice contraction is expected, leading to the shift of diffraction peaks to higher angles.^{39,42,50} However, in this system, we did not observe a significant change in peak position or width: this suggests that the crystallization process allows only a small fraction of Mn^{2+} to enter the $\text{NMA}_2\text{PbBr}_4$ lattice, without therefore resulting in sensible structural change or strain, regardless of the Mn concentration in the precursor solution.

Despite the minor structural changes, Mn addition has a clear impact on the optical properties. The $\text{NMA}_2\text{PbBr}_4$ absorption spectrum shows the sharp excitonic absorption typical of 2D perovskites peaked at 385 nm, further confirming the formation of the layered perovskite structure in which the exciton binding energy is strongly enhanced due to quantum and dielectric confinement effects. With Mn addition a clear, albeit small, 3 nm blue-shifts and 3 nm bandwidth broadening of the excitonic peak is observed (Fig. 1B and S2). A similar effect involving the blue-shift of the band-edge absorption was also reported in Mn-doped CsPbCl_3 and CdSe nanocrystals, and can be attributed to the substitutional alloying of Mn^{2+} in the PbBr_4^{2-} framework which partially disrupts the orbital hybridization of the inorganic skeleton of the host.^{42,57,58} The change in the absorption spectrum is extremely similar for all the doped films, irrespective of the Mn/Pb ratio, indicating that the lattice reaches saturation already at the lowest Mn concentration in the precursor solution.

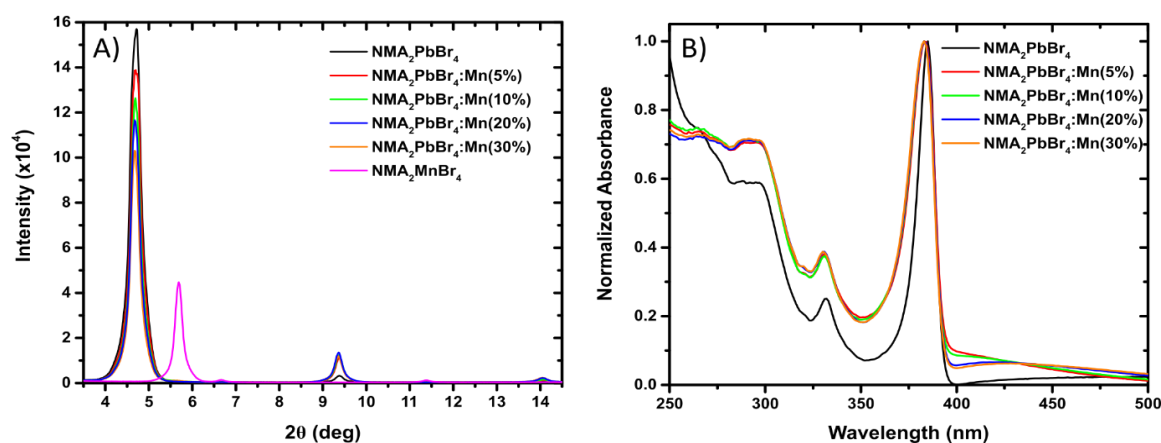


Figure 1. Impact of Mn addition to NMA₂PbBr₄. A) X-ray diffraction (XRD) patterns and B) normalized absorption spectra of NMA₂PbBr₄:Mn(x), with x = 0-30%.

While having minor effects on the perovskite absorption (see also temperature dependent absorption in Fig. S3), manganese inclusion heavily affects the luminescence properties of the material. Upon photoexcitation of NMA₂PbBr₄, the main free-excitonic emission is observed at 390 nm (3.18 eV), jointly with a broad luminescence tail in the range 400-500 nm, likely arising from intra-gap defect states with a wide energy distribution (Fig. 2a). Additionally, the broad triplet emission from the NMA⁺ organic cations appears as a weaker broad band peaked at 550 nm. On the other hand, in the doped films the free excitonic emission is almost completely quenched, while a bright orange emission (peaked at 600 nm) originating from the ⁴T₁ → ⁶A₁ transition in the 3d shell of the Mn²⁺ dominates the spectrum (Fig. 2b; see Fig. S8 for the detail of excitonic emission). We note that the quenching of the free-excitonic luminescence in favour of the Mn²⁺ emission is more marked than in Mn-doped CsPbCl_{x-3}Br₃ nanocrystals,^{42,50} indicating a more efficient energy transfer to the guest ions in the case of the 2D perovskite NMA₂PbBr₄. The change in emission wavelength is accompanied by a remarkable PLQY enhancement from less than 1% (pristine perovskite) up to 22% in doped perovskite thin films. Although we reached the maximum PLQY value at the Mn²⁺ concentration x=10% mol, we note that the PLQY is barely affected by the Mn²⁺ concentration in the precursor solution, and remains nearly constant (PLQY~20%) within the range x=2%-30% mol Mn²⁺ (Fig. S4). We have also tested the iodide-based perovskite NMA₂PbI₄. Here the NMA phosphorescence is not visible and Mn²⁺ doping is much less effective, since manganese emission only appears as a weak shoulder of the main free-excitonic emission (Fig. 2C,D). This observation is consistent with previous reports on CsPbX₃ nanocrystals, where the intensity of Mn luminescence decreases in the series Cl->Br->I following the reduction in thermodynamic driving force for the energy transfer to the doping centres. This is due to the perovskite band gap narrowing and the consequent unfavourable relative position of the energy levels of host and dopant.^{42,50}

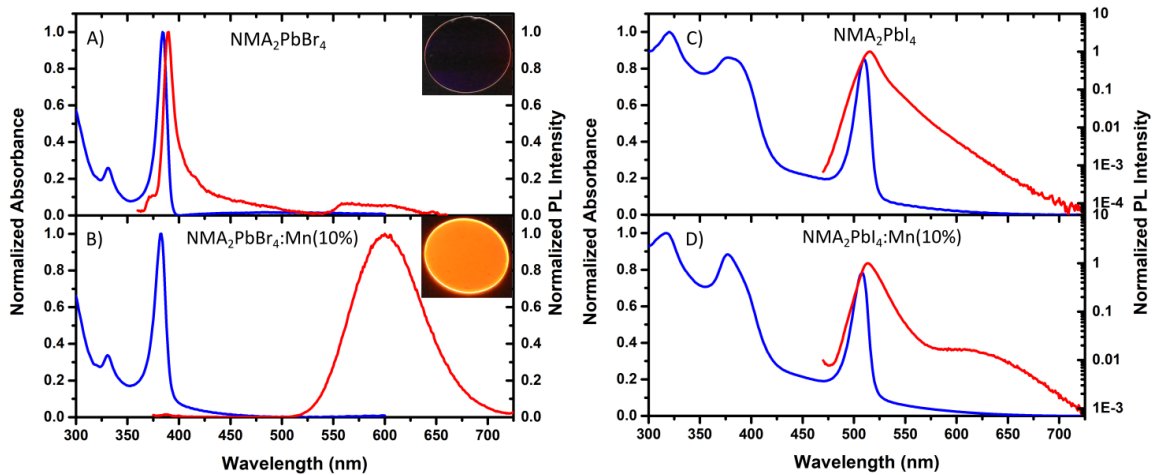


Figure 2. Doping effects on perovskite's photoluminescence. Normalized absorption (blue) and photoluminescence spectra (red) of A) $\text{NMA}_2\text{PbBr}_4$ - $\lambda_{\text{exc}}=340\text{nm}$; B) $\text{NMA}_2\text{PbBr}_4:\text{Mn}(10\%)$ - $\lambda_{\text{exc}}=365\text{nm}$; C) NMA_2PbI_4 - $\lambda_{\text{exc}}=450\text{nm}$; D) $\text{NMA}_2\text{PbI}_4:\text{Mn}(10\%)$ - $\lambda_{\text{exc}}=450\text{nm}$. The insets in (A,B) show the photoluminescence of non-doped and doped perovskite films under UV lamp excitation (366 nm).

Differently from the standard alkylammonium cations such as butylammonium, 1-naphthylmethylammonium (NMA) is a functional organic cation which enables an active role in the optoelectronic properties of the perovskite.^{12,36,37,54} In fact, the organic salt precursor (NMA)Br at room temperature shows intense fluorescence peaked at 350 nm jointly to a broad, weak phosphorescence in the range 550-650 nm (Fig. S5). When NMA is embedded in the perovskite lattice, the structural rigidification jointly with the heavy atom-effect (the presence of Pb and Br relaxes the spin selection rule for the formally forbidden $T_1 \rightarrow S_0$ transition) considerably enhance its phosphorescence, which becomes clearly visible (Fig. 3A).^{53,55} At low temperature the NMA triplet emission is further resolved, showing the vibronic progression of the phosphorescence with the main two transitions peaked at 560 nm and 605 nm (see also the normalized PL spectrum in Fig. S6). The photoexcitation map (Fig. 3B) shows an excellent match between the triplet emission band and the perovskite absorption profile, indicating transfer from the excitons in the PbBr_4^{2-} layers to the triplet of the organic layers. However, a closer look at the spectrum highlights a strong competition between the energy transfer towards the triplet state and the exciton trapping processes, leading to a broad PL tail in the range 400-500 nm. On the other hand, in $\text{NMA}_2\text{PbBr}_4:\text{Mn}(10\%)$ the Mn: ${}^4T_1 \rightarrow {}^6A_1$ luminescence undergoes a continuous redshift and narrowing when decreasing temperature (full width at half maximum, FWHM from 90 nm to 55 nm in the range 360K – 77K; Fig. 3C and Fig. S7); this is expected for substitutional doping where Mn^{2+} is in pseudo-octahedral coordination and lattice contraction at lower temperature results in the enhancement of crystal-field strength, thus decreasing the energy of the ${}^4T_1 \rightarrow {}^6A_1$ transition.^{51,59} The excitation spectrum of the transition based on the Mn 3d orbitals perfectly matches the perovskite absorption, indicating an excellent energy transfer from the perovskite host structure to the guest Mn^{2+} ions. Thanks to band narrowing and red-shift, at temperatures below 120K it is possible to disentangle the NMA phosphorescence from underneath the main broad manganese emission, appearing as a weaker shoulder at 560 nm. This reveals that both radiative channels remain active even in the doped system, with the Mn luminescence being the dominant component.

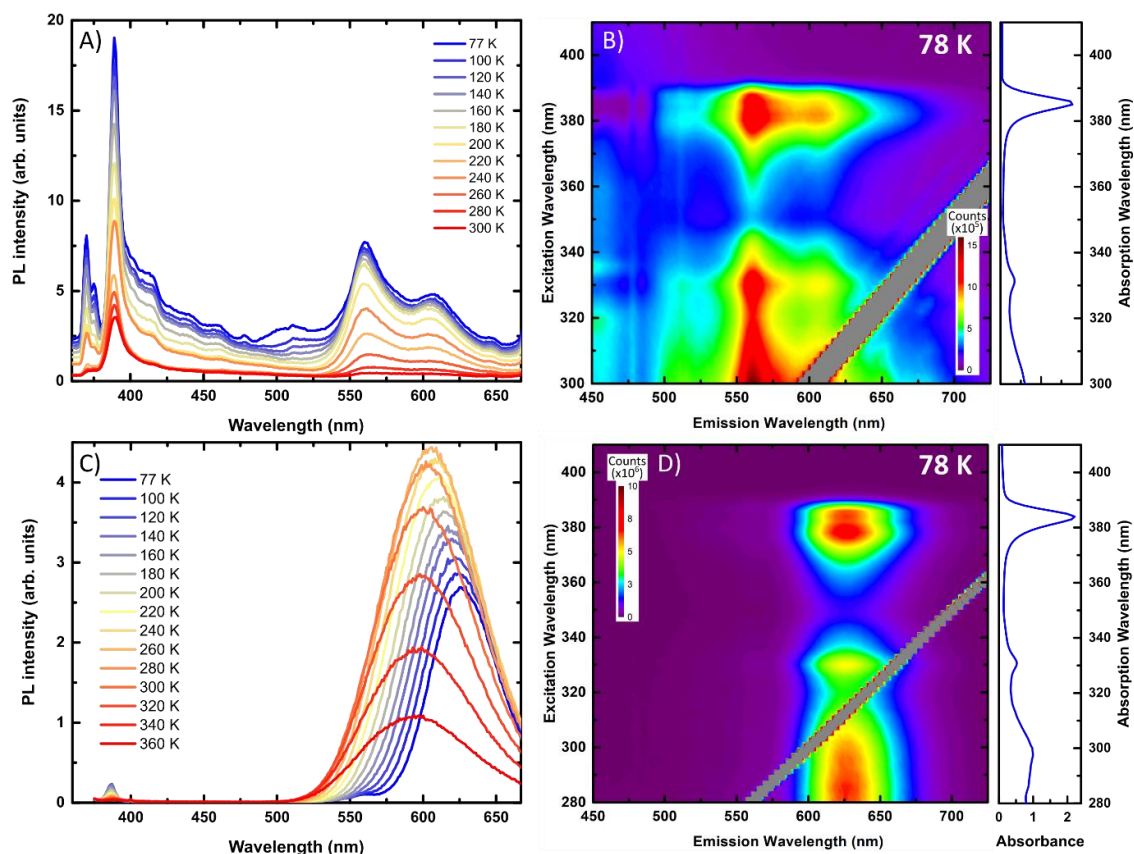


Figure 3. Temperature-dependent photoluminescence. $\text{NMA}_2\text{PbBr}_4$ A) temperature dependent PL ($\lambda_{\text{exc}}=340\text{nm}$) and B) photoexcitation map at 78 K. $\text{NMA}_2\text{PbBr}_4:\text{Mn}(10\%)$ C) temperature dependent PL ($\lambda_{\text{exc}}=365\text{nm}$) and D) photoexcitation map at 78 K.

Contrary to the perovskite's free excitonic emission, which decreases at higher temperature (Fig. 3C and S8), the temperature dependence of the manganese PL intensity shows a maximum at 260 K, which allows to identify two distinct regimes (Figure 4A). When $77\text{ K} < T < 260\text{ K}$ the Mn^{2+} emission increases at higher temperature, likely as a consequence of improved exciton diffusion from the perovskite to the emissive doping centres. Thanks to the favourable alignment of the NMA triplet state (T_1), transfer could proceed via two channels schematically depicted in the energy level diagram of Fig 4B: i) direct transfer from the perovskite's excitons to the recombination centres introduced by the Mn^{2+} guest; ii) cascade transfer from the perovskite's excitons to the NMA triplet state, followed by final transfer to the Mn^{2+} centres. Both mechanisms compete with the exciton trapping at the perovskite defect sites that, in the pristine material, result in PL broadening and promote non-radiative recombination causing severe luminescence quenching. In the doped system, funnelling to Mn^{2+} introduces an additional channel which allows to overcome the detrimental trapping at perovskite defects, favouring radiative recombination at the doping sites and finally enhancing the PLQY. When $T > 260\text{ K}$, the PL intensity quickly drops since de-trapping from Mn^{2+} sites become more favourable (likely involving back-transfer to the NMA triplet state, Fig. 4B), jointly with increased exciton thermal quenching up to 360 K (Fig. 4A). We also performed time-resolved photoluminescence measurements (TRPL) under photoexcitation at 355 nm (3.49 eV) at room temperature. The emission from $(\text{NMA})_2\text{PbBr}_4$ (Fig. 4C) decays in

few hundreds of μs , a typical time range for triplet excitation.⁵³ Upon manganese addition (Fig. 4D), the PL spectrum consists in a main band at 620 nm with a lifetime extended to thousands of μs , characteristic of the formally spin- and parity-forbidden ${}^4T_1 \rightarrow {}^6A_1$ transition of Mn^{2+} which slows down the radiative recombination.^{51,59} The power dependence of the manganese luminescence shows a maximum of relative PLQY at the excitation density 10^{17} cm^{-3} , which might stem from exciton-exciton annihilation processes occurring at higher excitations even before reaching the saturation of the Mn^{2+} emissive centres.

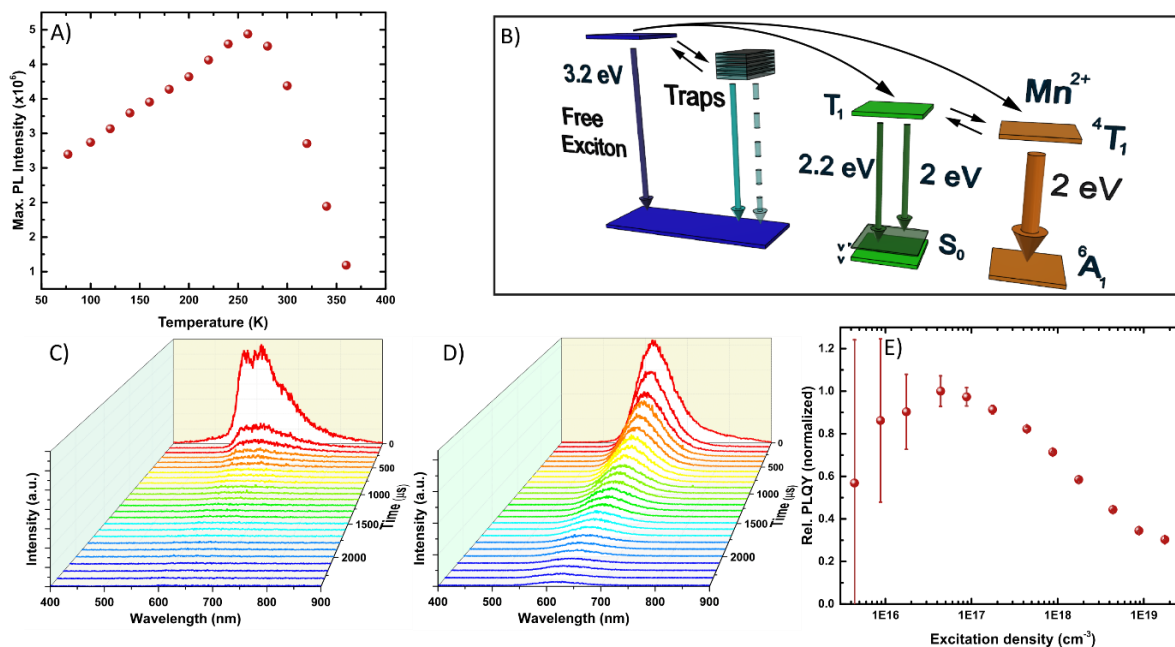


Figure 4. Transfer processes in the Mn-doped perovskite. A) Temperature dependence of the maximum photoluminescence intensity of $\text{NMA}_2\text{PbBr}_4:\text{Mn}(10\%)$; B) schematic representation of the energy level diagram in the Mn-doped system. The blue levels represent the perovskite's excitonic transition. The light-blue levels represent permanent traps with wide energy distribution, with the two arrows showing radiative (continuous line) and non-radiative (dashed line) recombination processes. T_1 and S_0 (green levels) are respectively the triplet and ground singlet state of NMA. The radiative transitions from T_1 to the two vibrational levels of S_0 (v and v') are represented, with energy 2.2 eV (560 nm) and 2.0 eV (605 nm). The orange levels represent the ${}^4T_1 \rightarrow {}^6A_1$ transition, based on the 3d orbitals of Mn^{2+} ; C) Time-resolved photoluminescence spectra of C) $\text{NMA}_2\text{PbBr}_4$ and D) $\text{NMA}_2\text{PbBr}_4:\text{Mn}(10\%)$. The time scales are in μs ; E) relative photoluminescence quantum yield (PLQY) against excitation density for $\text{NMA}_2\text{PbBr}_4:\text{Mn}(10\%)$.

To test the electroluminescence properties of the material, we integrated $(\text{NMA})_2\text{PbBr}_4:\text{Mn}(10\%)$ as emitter in a perovskite light-emitting diode (PeLED) architecture. The structure of the device was ITO/PEDOT:PSS/PolyTPD/ $\text{NMA}_2\text{PbBr}_4:\text{Mn}(10\%)$ /TPBi/Ba/Al, where PEDOT:PSS is a hole injecting layer, PolyTPD plays a role of a hole transporting material, while TPBi is an electron transporting material (see Fig. 5A). Due to the low conductivity of the wide band gap lead bromide perovskite, the use of extremely thin perovskite layers was compulsory to allow charge transport and radiative recombination within the perovskite film. Spin coating from low concentration (0.066 M) DMF perovskite solutions on PolyTPD yielded 30 nm thick films made of discontinuous perovskite islands (Fig. 5B,C). Although the imperfect coverage creates extra current-loss channels in the device, the presence of thin perovskite islands allowed us to probe radiative recombination of injected charges within the perovskite domains at room temperature (Fig. 5C). The shape of the EL spectrum (Fig. 5D) closely resembles the PL spectrum of the doped material, proving that the emission is mainly originating from

manganese centres, although a minor contribution from the NMA triplet emission might also be involved (See Fig. S9). A small red-shift (10 nm) of the EL with respect to the PL is most likely caused by different mechanisms of excitation responsible for both emissions. In PL the whole bulk of the material is excited uniformly, therefore states with a wide energy distribution are populated evenly. On the other hand, in the case of electrical excitation charge carriers preferentially populate states with the lowest energy, hence emission is red-shifted with respect to PL. Finally note that in Fig. S9, the EQE of a non-doped PeLED with the same architecture as the Mn-doped one is also presented. The diode employing $\text{NMA}_2\text{PbBr}_4$ without doping is almost one order of magnitude less efficient; this feature reflects well the measured PLQY values of both materials and supports the doping strategy as a possible way for luminescence tuning and efficiency improvement of 2D perovskites.

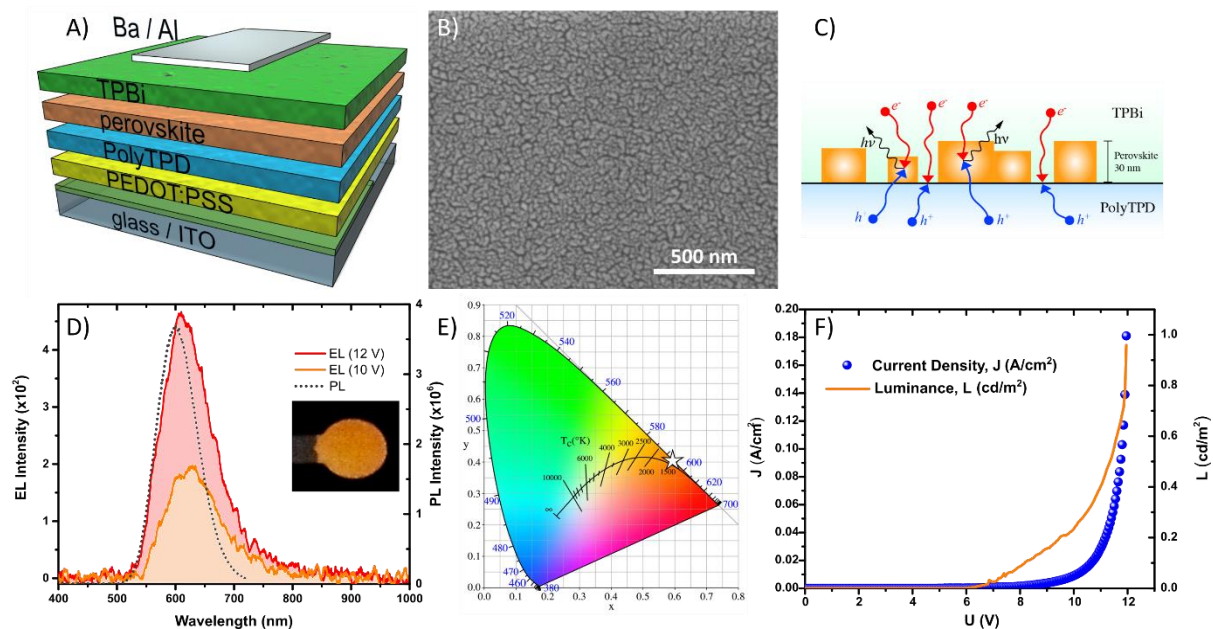


Figure 5. Perovskite integration in light-emitting diode (LED). A) LED architecture; B) SEM image of the $\text{NMA}_2\text{PbBr}_4:\text{Mn}(10\%)$ film morphology when deposited on top of PolyTPD; C) schematic representation of the island-like morphology of the perovskite film, with thickness $\sim 30\text{nm}$. The arrows represent electron (e^-) and hole (h^+) parasitic recombination at the PolyTPD/TPBi interface, as well as their radiative recombination within the perovskite domains; D) electroluminescence (EL) spectra measured in a $\text{NMA}_2\text{PbBr}_4:\text{Mn}(10\%)$ based LED, with the inset showing the orange emission from the device; E) CIE coordinates (0.59, 0.41) of the orange EL; F) Current density-voltage-luminance plot of the $\text{NMA}_2\text{PbBr}_4:\text{Mn}(10\%)$ LED.

CIE coordinates of the EL spectrum are $x = 0.59$, $y = 0.41$ (Fig. 5E), which correspond to orange colour, as confirmed by a photograph of the working device in the inset of Fig. 5D. Current density-voltage-luminance plot of the device is presented in Fig. 5F. The current density curve has the shape typical for a diode, while the luminance curve does not follow the same trend. Such discrepancy is probably caused by the poor conductive properties of the 2D perovskite and the not optimal electrical conditions for efficient emission from the material, which ultimately lead to low luminance values at relatively high current densities.

In summary, we have investigated the effects of Mn-doping in NMA_2PbX_4 , where NMA=1-naphthylmethylammonium and $X=\text{Br}, \text{I}$. Even though transfer from the perovskite inorganic layers can occur to both NMA and Mn^{2+} , we showed that only after manganese introduction a remarkable improvement of luminescence efficiency is achieved, reaching $\text{PLQY} > 22\%$ in doped films. This indicates that the insertion of the metallic heteroatom into the perovskite

framework is fundamental to guarantee highly efficient energy transfer to the doping centres overcoming trap-mediated non-radiative recombination pathways. For the first time, we have shown electroluminescence from the guest metallic ions (Mn^{2+}) in a perovskite host structure achieved in light-emitting diodes with room-temperature operability, with improved properties compared to the pristine perovskite. This proof-of-concept demonstration shows the effectiveness of inorganic doping as alternative way to tune and enhance the optoelectronic properties of layered perovskites, paving the way for the study of more efficient materials. Our work motivates the study of different combination of templating organic cations and metallic ion guests (e.g., Cu^+ and lanthanides) and prompts the deeper investigation of the transfer dynamics in such complex systems. We foresee that the development of new deposition methods to obtain uniform ultra-thin 2D perovskite films, and the use of multidimensional perovskites as host structures will considerably improve the charge transport as well as the device efficiency.

EXPERIMENTAL PROCEDURES

The experimental procedures are included in the Supplemental Information.

SUPPLEMENTAL INFORMATION

Supplemental Information includes Supplemental Experimental Procedures and 9 figures.

AUTHORS CONTRIBUTIONS

D.C. and W.M. contributed equally to this work. D. C. and A.P. conceived the idea for the manuscript and designed the experiments. D. C. synthesized and characterized the materials. W. M. fabricated and characterized the PeLEDs. S. N., T. B. and G. F. performed spectroscopic characterizations. A. P. supervised the work. All authors contributed to the data analysis, discussed the results and contributed to the writing of the manuscript.

ACKNOWLEDGEMENTS

This work has been in part funded by the ERC project SOPHY under grant agreement N 771528. We thank Alex J. Barker for technical support and Stefano Perissinotto for assistance in the SEM characterization.

REFERENCES AND NOTES

1. Birowosuto, M. D., Cortecchia, D., Drozdowski, W., Brylew, K., Lachmanski, W., Bruno, A., and Soci, C. (2016). X-ray scintillation in lead halide perovskite crystals. *Sci. Rep.* *6*, 37254.
2. Cegielski, P. J., Neutzner, S., Porschatis, C., Lerch, H., Bolten, J., Suckow, S., Kandada, A. R. S., Chmielak, B., Petrozza, A., Wahlbrink, T., and Giesecke, A. L. (2017). Integrated perovskite lasers on a silicon nitride waveguide platform by cost-effective high throughput fabrication. *Opt. Express* *25*, 13199.
3. Chin, X. Y., Cortecchia, D., Yin, J., Bruno, A., and Soci, C. (2015). Lead iodide perovskite light-emitting field-effect transistor. *Nat. Commun.* *6*, 7383.
4. Sutherland, B. R. and Sargent, E. H. (2016). Perovskite photonic sources. *Nat. Photon.* *10*, 295.
5. Veldhuis, S. A., Boix, P. P., Yantara, N., Li, M., Sum, T. C., Mathews, N., and Mhaisalkar, S. G. (2016). Perovskite materials for light-emitting diodes and lasers. *Adv. Mater.* *28*, 6804.

6. Adjokatse, S., Fang, H.-H., and Loi, M. A. (2017). Broadly tunable metal halide perovskites for solid-state light-emission applications. *Mat. Today* *20*, 413.
7. Maddalena, F., Chin, X. Y., Cortecchia, D., Bruno, A., and Soci, C. (2018). Brightness enhancement in pulsed-operated perovskite light-emitting transistors. *ACS Appl. Mater. Interfaces*.
8. Green, M. A. and Ho-Baillie, A. (2017). Perovskite solar cells: the birth of a new era in photovoltaics. *ACS Energy Lett.* *2*, 822.
9. Lin, K., Xing, J., Quan, L. N., de Arquer, F. P. G., Gong, X., Lu, J., Xie, L., Zhao, W., Zhang, D., Yan, C., Li, W., Liu, X., Lu, Y., Kirman, J., Sargent, E. H., Xiong, Q., and Wei, Z. (2018). Perovskite light-emitting diodes with external quantum efficiency exceeding 20 per cent. *Nature* *562*, 245.
10. Cao, Y., Wang, N., Tian, H., Guo, J., Wei, Y., Chen, H., Miao, Y., Zou, W., Pan, K., He, Y., Cao, H., Ke, Y., Xu, M., Wang, Y., Yang, M., Du, K., Fu, Z., Kong, D., Dai, D., Jin, Y., Li, G., Li, H., Peng, Q., Wang, J., and Huang, W. (2018). Perovskite light-emitting diodes based on spontaneously formed submicrometre-scale structures. *Nature* *562*, 249.
11. Chiba, T., Hayashi, Y., Ebe, H., Hoshi, K., Sato, J., Sato, S., Pu, Y.-J., Ohisa, S., and Kido, J. (2018). Anion-exchange red perovskite quantum dots with ammonium iodine salts for highly efficient light-emitting devices. *Nat. Photon.* *12*, 681.
12. Saparov, B. and Mitzi, D. B. (2016). Organic–inorganic perovskites: structural versatility for functional materials design. *Chem. Rev.* *116*, 4558.
13. Xing, G., Wu, B., Wu, X., Li, M., Du, B., Wei, Q., Guo, J., Yeow, E. K. L., Sum, T. C., and Huang, W. (2017). Transcending the slow bimolecular recombination in lead-halide perovskites for electroluminescence. *Nat. Commun.* *8*, 14558.
14. Even, J., Pedesseau, L., and Katan, C. (2014). Understanding quantum confinement of charge carriers in layered 2D hybrid perovskites. *ChemPhysChem* *15*, 3733.
15. Ishihara, T., Takahashi, J., and Goto, T. (1989). Exciton state in two-dimensional perovskite semiconductor $(\text{C}_{10}\text{H}_{21}\text{NH}_3)_2\text{PbI}_4$. *Solid State Commun.* *69*, 933.
16. Cortecchia, D., Lew, K. C., So, J.-K., Bruno, A., and Soci, C. (2017). Cathodoluminescence of self-organized heterogeneous phases in multidimensional perovskite thin films. *Chem. Mater.* *29*, 10088.
17. Wang, N., Cheng, L., Ge, R., Zhang, S., Miao, Y., Zou, W., Yi, C., Sun, Y., Cao, Y., Yang, R., Wei, Y., Guo, Q., Ke, Y., Yu, M., Jin, Y., Liu, Y., Ding, Q., Di, D., Yang, L., Xing, G., Tian, H., Jin, C., Gao, F., Friend, R. H., Wang, J., and Huang, W. (2016). Perovskite light-emitting diodes based on solution-processed self-organized multiple quantum wells. *Nat. Photon.* *10*, 699.
18. Yang, X., Zhang, X., Deng, J., Chu, Z., Jiang, Q., Meng, J., Wang, P., Zhang, L., Yin, Z., and You, J. (2018). Efficient green light-emitting diodes based on quasi-two-dimensional composition and phase engineered perovskite with surface passivation. *Nat. Commun.* *9*, 570.
19. Yantara, N., Bruno, A., Iqbal, A., Jamaludin, N. F., Soci, C., Mhaisalkar, S., and Mathews, N. (2018). Designing efficient energy funneling kinetics in ruddlesden–popper perovskites for high-performance light-emitting diodes. *Adv. Mater.* *30*, 1800818.
20. Yuan, M., Quan, L. N., Comin, R., Walters, G., Sabatini, R., Voznyy, O., Hoogland, S., Zhao, Y., Beauregard, E. M., Kanjanaboos, P., Lu, Z., Kim, D. H., and Sargent, E. H. (2016). Perovskite energy funnels for efficient light-emitting diodes. *Nat. Nanotech.* *11*, 872.
21. Zhang, S., Yi, C., Wang, N., Sun, Y., Zou, W., Wei, Y., Cao, Y., Miao, Y., Li, R., Yin, Y., Zhao, N., Wang, J., and Huang, W. (2017). Efficient red perovskite light-emitting diodes based on solution-processed multiple quantum wells. *Adv. Mater.* *29*, 1606600.
22. Quan, L. N., Zhao, Y., García de Arquer, F. P., Sabatini, R., Walters, G., Voznyy, O., Comin, R., Li, Y., Fan, J. Z., Tan, H., Pan, J., Yuan, M., Bakr, O. M., Lu, Z., Kim, D. H., and Sargent, E. H. (2017). Tailoring the energy landscape in quasi-2D halide perovskites enables efficient green-light emission. *Nano Lett.* *17*, 3701.
23. Gong, X., Voznyy, O., Jain, A., Liu, W., Sabatini, R., Piontkowski, Z., Walters, G., Bappi, G., Nokhrin, S., Bushuyev, O., Yuan, M., Comin, R., McCamant, D., Kelley, S. O., and Sargent, E. H. (2018). Electron–phonon interaction in efficient perovskite blue emitters. *Nat. Mater.* *17*, 550.

24. Cortecchia, D., Neutzner, S., Srimath Kandada, A. R., Mosconi, E., Meggiolaro, D., De Angelis, F., Soci, C., and Petrozza, A. (2017). Broadband emission in two-dimensional hybrid perovskites: the role of structural deformation. *J. Am. Chem. Soc.* *139*, 39.
25. Koutselas, I., Bampoulis, P., Maratou, E., Evagelinou, T., Pagona, G., and Papavassiliou, G. C. (2011). Some unconventional organic–inorganic hybrid low-dimensional semiconductors and related light-emitting devices. *J. Phys. Chem. C* *115*, 8475.
26. Lanzetta, L., Marin-Beloqui, J. M., Sanchez-Molina, I., Ding, D., and Haque, S. A. (2017). Two-dimensional organic tin halide perovskites with tunable visible emission and their use in light-emitting devices. *ACS Energy Lett.* *2*, 1662.
27. Liang, D., Peng, Y., Fu, Y., Shearer, M. J., Zhang, J., Zhai, J., Zhang, Y., Hamers, R. J., Andrew, T. L., and Jin, S. (2016). Color-pure violet-light-emitting diodes based on layered lead halide perovskite nanoplates. *ACS Nano* *10*, 6897.
28. Vassilakopoulou, A., Papadatos, D., and Koutselas, I. (2016). Room temperature light emitting diode based on 2D hybrid organic-inorganic low dimensional perovskite semiconductor. *Appl. Mater. Today* *5*, 128.
29. Kawano, N., Koshimizu, M., Sun, Y., Yahaba, N., Fujimoto, Y., Yanagida, T., and Asai, K. (2014). Effects of organic moieties on luminescence properties of organic–inorganic layered perovskite-type compounds. *J. Phys. Chem. C* *118*, 9101.
30. Era, M., Morimoto, S., Tsutsui, T., and Saito, S. (1994). Organic-inorganic heterostructure electroluminescent device using a layered perovskite semiconductor $(\text{C}_6\text{H}_5\text{C}_2\text{H}_4\text{NH}_3)_2\text{PbI}_4$. *Appl. Phys. Lett.* *65*, 676.
31. Chong, W. K., Thirumal, K., Giovanni, D., Goh, T. W., Liu, X., Mathews, N., Mhaisalkar, S., and Sum, T. C. (2016). Dominant factors limiting the optical gain in layered two-dimensional halide perovskite thin films. *Phys. Chem. Chem. Phys.* *18*, 14701.
32. Gauthron, K., Lauret, J. S., Doyennette, L., Lanty, G., Al Choueiry, A., Zhang, S. J., Brehier, A., Largeau, L., Mauguin, O., Bloch, J., and Deleporte, E. (2010). Optical spectroscopy of two-dimensional layered $(\text{C}_6\text{H}_5\text{C}_2\text{H}_4\text{NH}_3)_2\text{PbI}_4$ perovskite. *Opt. Express* *18*, 5912.
33. Hong, X., Ishihara, T., and Nurmikko, A. V. (1992). Dielectric confinement effect on excitons in PbI_4 -based layered semiconductors. *Phys. Rev. B* *45*, 6961.
34. Cortecchia, D., Yin, J., Bruno, A., Lo, S.-Z. A., Gurzadyan, G. G., Mhaisalkar, S., Brédas, J.-L., and Soci, C. (2017). Polaron self-localization in white-light emitting hybrid perovskites. *J. Mat. Chem. C* *5*, 2771.
35. Chondroudis, K. and Mitzi, D. B. (1999). Electroluminescence from an Organic–Inorganic Perovskite Incorporating a Quaterthiophene Dye within Lead Halide Perovskite Layers. *Chem. Mater.* *11*, 3028.
36. Cortecchia, D., Soci, C., Cametti, M., Petrozza, A., and Martí-Rujas, J. (2017). Crystal engineering of a two-dimensional lead-free perovskite with functional organic cations by second-sphere coordination. *ChemPlusChem* *82*, 681.
37. Mitzi, D. B., Chondroudis, K., and Kagan, C. R. (1999). Design, Structure, and Optical Properties of Organic–Inorganic Perovskites Containing an Oligothiophene Chromophore. *Inorg. Chem.* *38*, 6246.
38. Akkerman, Q. A., Meggiolaro, D., Dang, Z., De Angelis, F., and Manna, L. (2017). Fluorescent Alloy $\text{CsPb}_x\text{Mn}_{1-x}\text{I}_3$ Perovskite Nanocrystals with High Structural and Optical Stability. *ACS Energy Lett.* *2*, 2183.
39. Chen, D., Fang, G., Chen, X., Lei, L., Zhong, J., Mao, Q., Zhou, S., and Li, J. (2018). Mn-Doped CsPbCl_3 perovskite nanocrystals: solvothermal synthesis, dual-color luminescence and improved stability. *J. Mat. Chem. C* *6*, 8990.
40. Kroupa, D. M., Roh, J. Y., Milstein, T. J., Creutz, S. E., and Gamelin, D. R. (2018). Quantum-cutting ytterbium-doped $\text{CsPb}(\text{Cl}_{1-x}\text{Br}_x)_3$ perovskite thin films with photoluminescence quantum yields over 190%. *ACS Energy Lett.*, 2390.
41. Lin, C. C., Xu, K. Y., Wang, D., and Meijerink, A. (2017). Luminescent manganese-doped CsPbCl_3 perovskite quantum dots. *Sci. Rep.* *7*, 45906.

42. Liu, W., Lin, Q., Li, H., Wu, K., Robel, I., Pietryga, J. M., and Klimov, V. I. (2016). Mn²⁺-doped lead halide perovskite nanocrystals with dual-color emission controlled by halide content. *J. Am. Chem. Soc.* *138*, 14954.
43. Meinardi, F., Akkerman, Q. A., Bruni, F., Park, S., Mauri, M., Dang, Z., Manna, L., and Brovelli, S. (2017). Doped halide perovskite nanocrystals for reabsorption-free luminescent solar concentrators. *ACS Energy Lett.* *2*, 2368.
44. Milstein, T. J., Kroupa, D. M., and Gamelin, D. R. (2018). Picosecond quantum cutting generates photoluminescence quantum yields over 100% in ytterbium-doped CsPbCl₃ nanocrystals. *Nano Lett.* *18*, 3792.
45. Pan, G., Bai, X., Yang, D., Chen, X., Jing, P., Qu, S., Zhang, L., Zhou, D., Zhu, J., Xu, W., Dong, B., and Song, H. (2017). Doping lanthanide into perovskite nanocrystals: highly improved and expanded optical properties. *Nano Lett.* *17*, 8005.
46. Parobek, D., Roman, B. J., Dong, Y., Jin, H., Lee, E., Sheldon, M., and Son, D. H. (2016). Exciton-to-dopant energy transfer in Mn-doped cesium lead halide perovskite nanocrystals. *Nano Lett.* *16*, 7376.
47. Xu, K., Lin, C. C., Xie, X., and Meijerink, A. (2017). Efficient and stable luminescence from Mn²⁺ in core and core–isocrystalline shell CsPbCl₃ perovskite nanocrystals. *Chem. Mater.* *29*, 4265.
48. Zhou, D., Liu, D., Pan, G., Chen, X., Li, D., Xu, W., Bai, X., and Song, H. (2017). Cerium and ytterbium codoped halide perovskite quantum dots: a novel and efficient downconverter for improving the performance of silicon solar cells. *Adv. Mater.* *29*, 1704149.
49. Zou, S., Liu, Y., Li, J., Liu, C., Feng, R., Jiang, F., Li, Y., Song, J., Zeng, H., Hong, M., and Chen, X. (2017). Stabilizing cesium lead halide perovskite lattice through Mn(II) substitution for air-stable light-emitting diodes. *J. Am. Chem. Soc.* *139*, 11443.
50. Guria, A. K., Dutta, S. K., Adhikari, S. D., and Pradhan, N. (2017). Doping Mn²⁺ in lead halide perovskite nanocrystals: successes and challenges. *ACS Energy Lett.* *2*, 1014.
51. Yuan, X., Ji, S., De Siena, M. C., Fei, L., Zhao, Z., Wang, Y., Li, H., Zhao, J., and Gamelin, D. R. (2017). Photoluminescence Temperature Dependence, Dynamics, and Quantum Efficiencies in Mn²⁺-Doped CsPbCl₃ Perovskite Nanocrystals with Varied Dopant Concentration. *Chem. Mater.* *29*, 8003.
52. Biswas, A., Bakthavatsalam, R., and Kundu, J. (2017). Efficient exciton to dopant energy transfer in Mn²⁺-doped (C₄H₉NH₃)₂PbBr₄ two-dimensional (2D) layered perovskites. *Chem. Mater.* *29*, 7816.
53. Baroncini, M., Bergamini, G., and Ceroni, P. (2017). Rigidification or interaction-induced phosphorescence of organic molecules. *Chem. Commun.* *53*, 2081.
54. Ema, K., Inomata, M., Kato, Y., Kunugita, H., and Era, M. (2008). Nearly perfect triplet-triplet energy transfer from wannier excitons to naphthalene in organic-inorganic hybrid quantum-well materials. *Phys. Rev. Lett.* *100*, 257401.
55. Era, M., Maeda, K., and Tsutsui, T. (1998). Enhanced phosphorescence from naphthalene-chromophore incorporated into lead bromide-based layered perovskite having organic–inorganic superlattice structure. *Chem. Phys. Lett.* *296*, 417.
56. Priestley, E. B. and Haug, A. (1968). Phosphorescence spectrum of pure crystalline naphthalene. *J. Chem. Phys.* *49*, 622.
57. Vlaskin, V. A., Barrows, C. J., Erickson, C. S., and Gamelin, D. R. (2013). Nanocrystal diffusion doping. *J. Am. Chem. Soc.* *135*, 14380.
58. Zhang, L., Geng, W., Tong, C.-j., Chen, X., Cao, T., and Chen, M. (2018). Strain induced electronic structure variation in methyl-ammonium lead iodide perovskite. *Sci. Rep.* *8*, 7760.
59. Xu, K. and Meijerink, A. (2018). Tuning Exciton–Mn²⁺ Energy Transfer in Mixed Halide Perovskite Nanocrystals. *Chem. Mater.* *30*, 5346.

Supplemental Information

Mn(II)-doped 2D perovskite for light emitting devices

Daniele Cortecchia, Wojciech Mróz, Stefanie Neutzner, Tetiana Borzda, Giulia Folpini
Annamaria Petrozza

Istituto Italiano di Tecnologia, Milan, 20133, Italy

1 Experimental methods

1.1 Materials.

1-Naphtylmethylamine (97%, Sigma Aldrich), lead bromide PbBr_2 (TCI), lead iodide PbI_2 (TCI), dimethylformamide DMF (anhydrous, Sigma Aldrich), hydriodic acid HI (57% in water, stabilized), hydrobromic acid HBr (48% in water, Sigma Aldrich), tetrahydrofuran THF (99.9%, Sigma Aldrich), chlorobenzene CB (anhydrous, Sigma Aldrich), dichloromethane DCM (anhydrous, Sigma Aldrich), poly(3,4-ethylenedioxythiophene) polystyrene sulfonate PEDOT:PSS (Heraeus Clevis P VP AI 4083), Poly[N,N'-bis(4-butylphenyl)-N,N'-bis(phenyl)-benzidine] PolyTPD (Ossila), 1,3,5-Tris(1-phenyl-1-H-benzimidazol-2-yl)benzene TPBi (Ossila), E132 PV & LED Encapsulation Epoxy (Ossila).

1.2 Synthesis of 1-naphtylmethylammonium bromide (NMA)Br and iodide (NMA)I.

1-Naphtylmethylamine (1.5 ml, 0.01 mmol) was dissolved in 40 ml of tetrahydrofuran (THF) and 3.3 ml of HBr 48% (3 equivalents) were added dropwise to the solution kept in an ice bath under vigorous magnetic stirring. The reaction was stopped after 3h, and the product was precipitated from THF by adding dichloromethane (DCM). This washing procedure was repeated 3 times, and the final product (NMA)Br was collected in form of a white powder by drying it under vacuum at 60 °C in a rotary evaporator. A similar synthetic procedure was adopted for (NMA)I, by substituting HBr with HI (57% water solution, stabilized).

1.3 Perovskite synthesis.

For the synthesis of the perovskite $\text{NMA}_2\text{PbBr}_4$, (NMA)Br and PbBr_2 were mixed in 2:1 molar ratio in dimethylformamide (DMF) in the desired concentration (typically 0.25M for thin films used for optical characterization). In the case of the doped perovskite $\text{NMA}_2\text{PbBr}_4\text{:Mn}(x\%)$, MnBr_2 was added to the precursor solution in the desired stoichiometric ratio, with the manganese content varying from 2% to 30% of the lead content. For example, in the case of $\text{NMA}_2\text{PbBr}_4\text{:Mn}(10\%)$, 0.25M solutions were prepared by mixing 59.5 mg (0.25 mmol) of (NMA)Br, 45.9 mg (0.125 mmol) of PbBr_2 and 2.68 mg (0.0125 mmol) MnBr_2 in 0.5 ml of DMF. $\text{NMA}_2\text{PbI}_4\text{:Mn}(10\%)$ were synthesized in a similar way by mixing (NMA)I, PbI_2 and MnBr_2 . The mixture was heated at 100 °C for 2h, and then spin coated on quartz substrates at 4000 rpm for 30 s, and the resulting film was annealed at 100 °C for 15 min. In the case of $\text{NMA}_2\text{PbBr}_4$ powders, the precursor DMF solution was dried under vacuum at 80 °C in a rotary evaporator, and finally annealed at 100°C for 4 h in vacuum oven.

1.4 Structural and morphological characterization.

Perovskite powders and thin films were characterized through X-ray diffraction (XRD) using a BRUKER D8 ADVANCE with Bragg-Brentano geometry, Cu K α radiation ($\lambda = 1.54056 \text{ \AA}$), step increment of 0.02° and 1 s of acquisition time. Films used for XRD analysis were spin coated from 0.25M solutions in DMF. The surface profiler Dektak 150 (Veeco) was used to measure the film thickness. The scanning electron microscope (SEM) MIRA3, TESCAN was used to characterize the film morphology. Before characterization, 7 nm of gold were evaporated on top of the thin film to avoid charging effects during the image acquisition.

1.5 Spectroscopic characterization.

Steady state absorption spectra were measured on perovskite thin films deposited on quartz using a UV/VIS/NIR spectrophotometer Lambda 1050, Perkin Elmer equipped with integrating sphere (module 150mm InGaAs Int. Sphere). Photoluminescence emission spectra were taken with a NanoLog (Horiba Jobin Yvon), while the absolute photoluminescence quantum yield (PLQY) was measured using an integrating sphere (Quanta- ϕ) in combination with the NanoLog spectrofluorometer. Low temperature measurements were performed in an Oxford Instruments cold finger cryostat MicrostatHEcooled with liquid nitrogen. Time-resolved photoluminescence measurements were performed by exciting the sample with the 3rd harmonic (355 nm) from a Nd:YAG Picolo-AOT laser with a pulse length of approximately 1000 ps and pulse fluence of $120 \mu\text{J}/\text{cm}^2$. The PL was detected with an Andor iStar 320T ICCD camera coupled to a Shamrock 303i spectrograph using a temporal step size of $100 \mu\text{s}$ and a spectral resolution of 0.2 nm. All measurements were performed in vacuum. The power dependent photoluminescence measurements were taken on thin films, deposited on sapphire to guarantee good thermal contact. The same light source as for the time-resolved photoluminescence measurements was used (Picolo-AOT) with 355 nm excitation wavelength. During the measurements, the sample was kept in the cold finger cryostat at 260 K to prevent sample degradation.

1.6 Fabrication of light-emitting diodes (LEDs).

Glass substrates with indium tin oxide (ITO) were etched with Zn powder and 2M HCl. The etched substrates were cleaned ultrasonically in distilled water, acetone and isopropanol and subsequently O_2 plasma treated for 10 min. Afterwards, poly(3,4-ethylenedioxythiophene) polystyrene sulfonate (Heraeus Clevis P VP AI 4083) (PEDOT:PSS) was spin-coated through PVDF filter (pore size $0.22 \mu\text{m}$) on substrates rotating 4000rpm, followed by thermal annealing at 110°C for 10 min in air. The deposited PEDOT:PSS layers had thicknesses around 50 nm. Then substrates were transferred to a N_2 filled glovebox where the rest of devices' construction processing followed. A chlorobenzene solution of Poly[N,N'-bis(4-butylphenyl)-N,N'-bis(phenyl)-benzidine] (PolyTPD) with concentration 15 mg/ml was spin-coated on PEDOT:PSS with 4000 rpm, resulting in a film of 25 nm thickness. The film was annealed at 100°C for 10 min and subsequently O_2 plasma treatment was applied for 5 s (outside the glovebox) to improve wettability of the PolyTPD film. On such substrates a hot (100°C) 0.066 M dimethyl formaldehyde (DMF) solution of $(\text{NMA})_2\text{PbBr}_4:\text{Mn}(10\%)$ was spin-coated with 6000 rpm and devices were annealed at 100°C for 15 min, achieving a final film thickness of

about 30 nm. Afterwards, a 35 nm thick film of 1,3,5-Tris(1-phenyl-1-H-benzimidazol-2-yl)benzene (TPBi) was thermally evaporated on the samples at a pressure 1×10^{-6} mbar. Subsequently, the samples were transferred to a metal evaporator, where 7 nm of barium and 100 nm of aluminium were evaporated through a shadow mask, creating in this way a cathode. The active area of the devices was 8.3 mm^2 . The light-emitting diodes were encapsulated by placing a single drop of a resin (E132 PV & LED Encapsulation Epoxy, Ossila) on the active area, covering it with a microscope glass slide and UV curing for 20 min.

1.7 Device characterization.

Current–voltage (I–V) device characterization was performed with a Keithley 2602 source meter combined with a photodiode with known responsivity (OSI Optoelectronics, UV-100DQC). Measurements were realized by applying bias to the diode while the photodiode in contact with the device registered the emitted light. Electroluminescence was collected by an optical fiber and recorded by an Ocean Optics Maya 2000 Pro spectrometer. Efficiencies were calculated assuming a Lambertian distribution of emission.

2 Supporting figures.

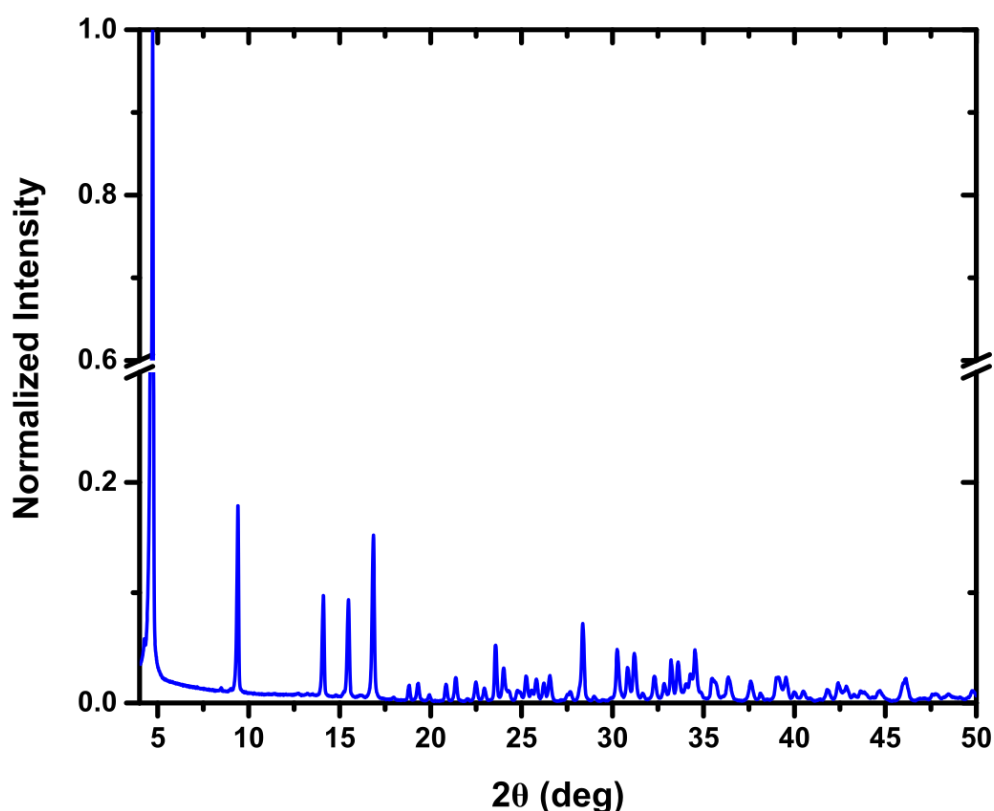


Figure S6. (NMA)₂PbBr₄ powder XRD.

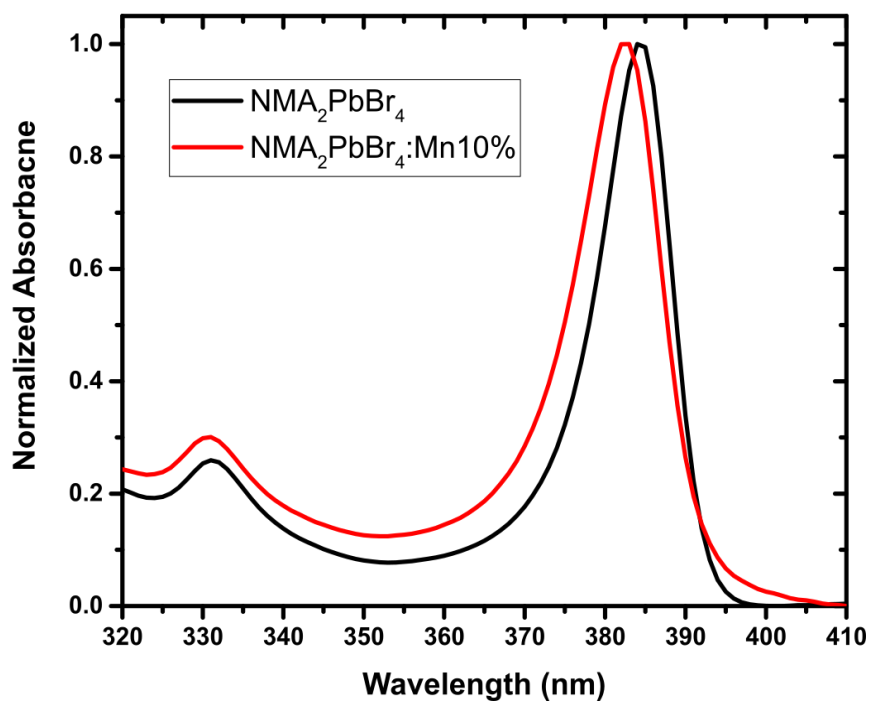


Figure S7. NMA₂PbBr₄ (black line) and NMA₂PbBr₄:Mn(10%) room temperature absorption spectra, showing a ~3 nm blue-shift and ~3 nm broadening of the excitonic absorption in the doped perovskite film.

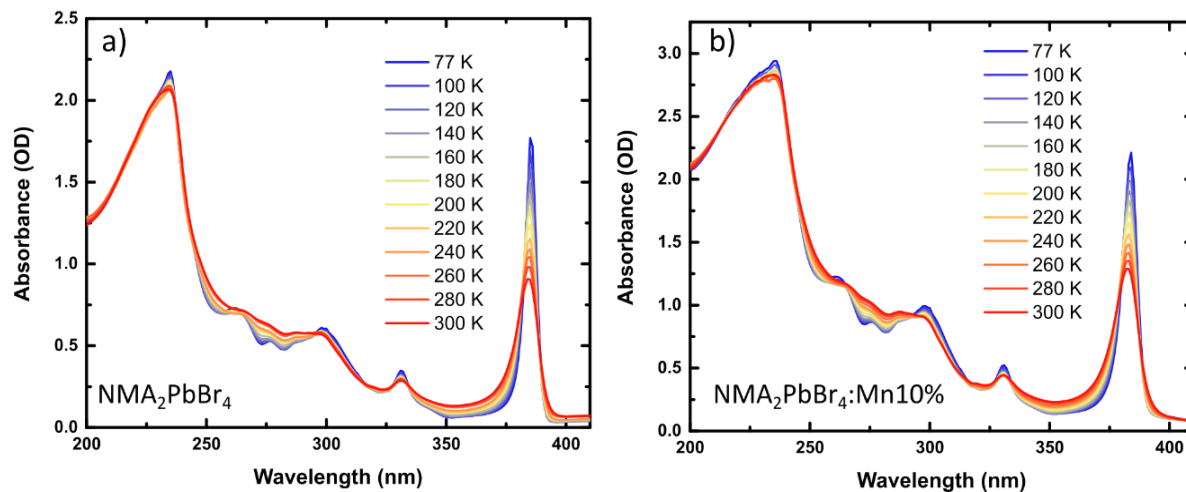


Figure S3. Temperature dependent absorption of a) NMA₂PbBr₄ and b) NMA₂PbBr₄:Mn(10%) thin films.

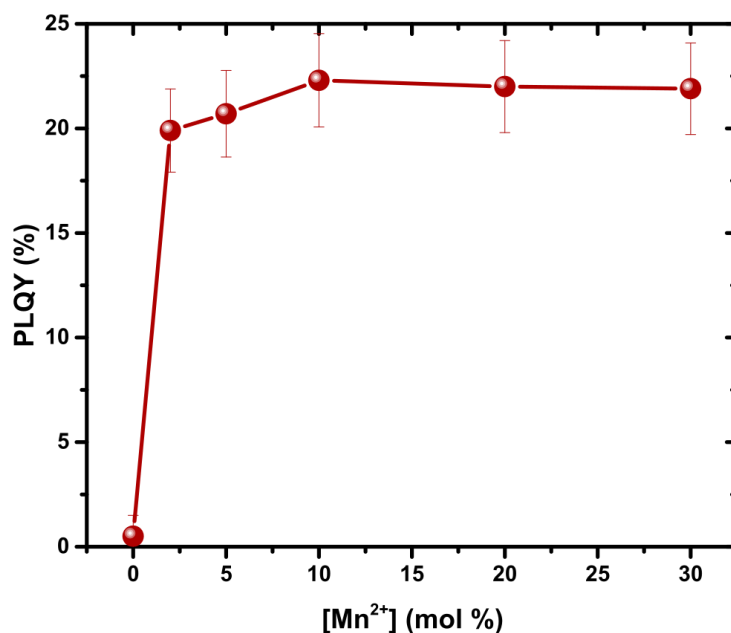


Figure S4. Dependency of the photoluminescence quantum yield (PLQY) of $\text{NMA}_2\text{PbBr}_4:\text{Mn}(x)$ on the Mn^{2+} content of the starting reaction solution. This is expressed as $x=0\text{-}30\%$ mol, indicating the Mn^{2+} molar content respect to the lead amount. The PLQYs of both $\text{NMA}_2\text{PbBr}_4$ and NMA_2PbI_4 pristine perovskites were estimated to be $< 1\%$, in a range comparable to or below the instrumental resolution.

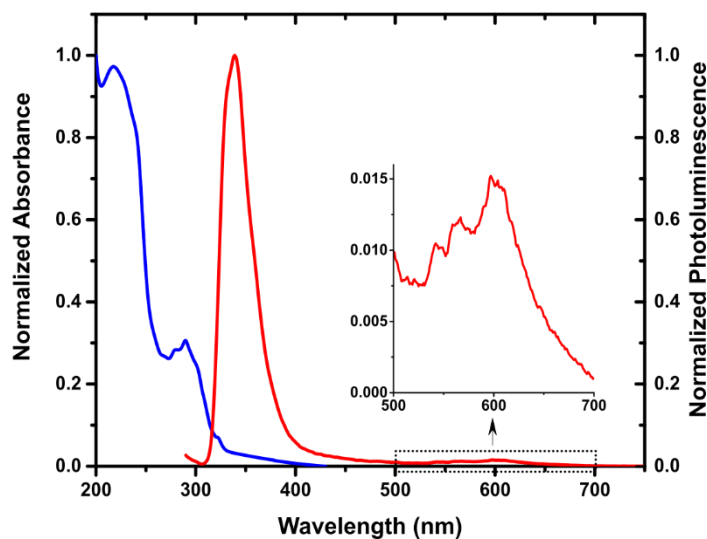


Figure S5. Absorption (blue line) and photoluminescence (red line) of the organic salt (NMA)Br at $\lambda_{\text{exc}}=270$ nm.

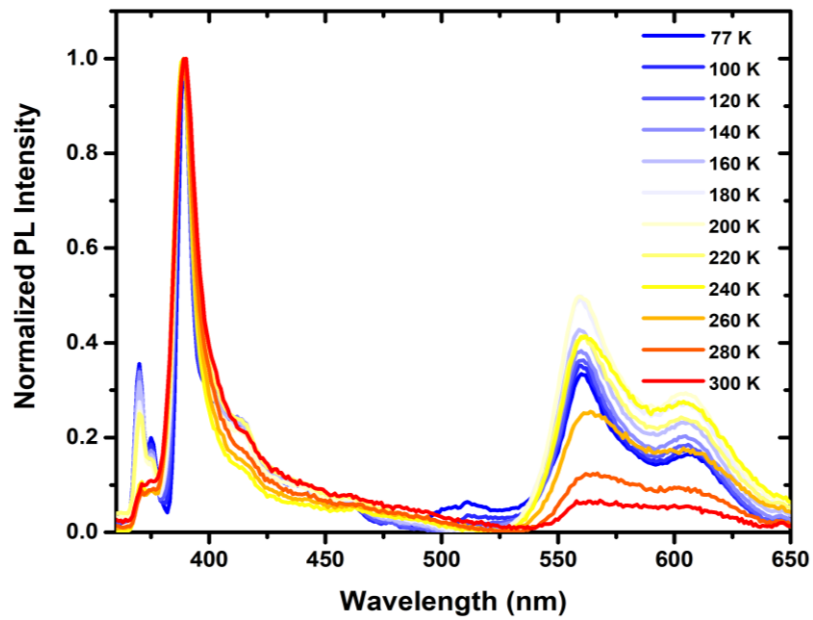


Figure S6. Temperature dependent, normalized photoluminescence of NMA₂PbBr₄. Excitation wavelength $\lambda_{\text{exc}}=340$ nm.

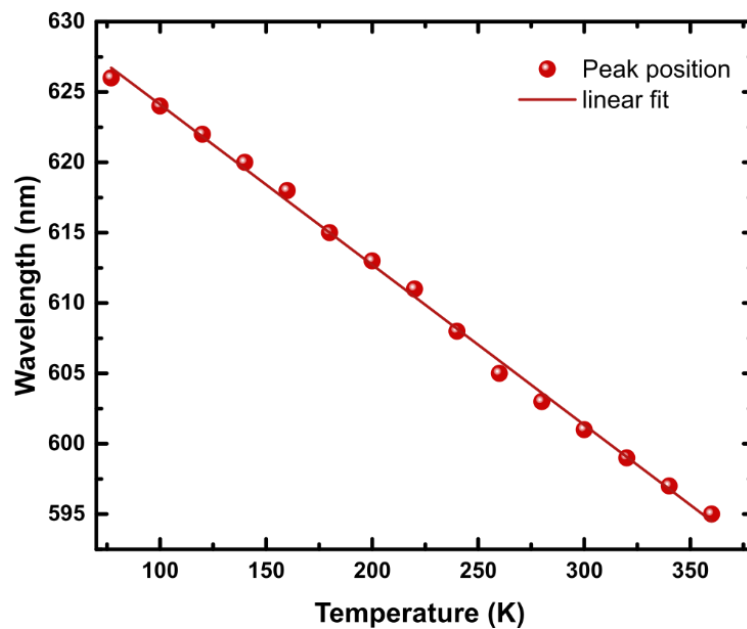


Figure S7. Temperature dependent shift of the photoluminescence peak maximum in NMA₂PbBr₄:Mn(10%).

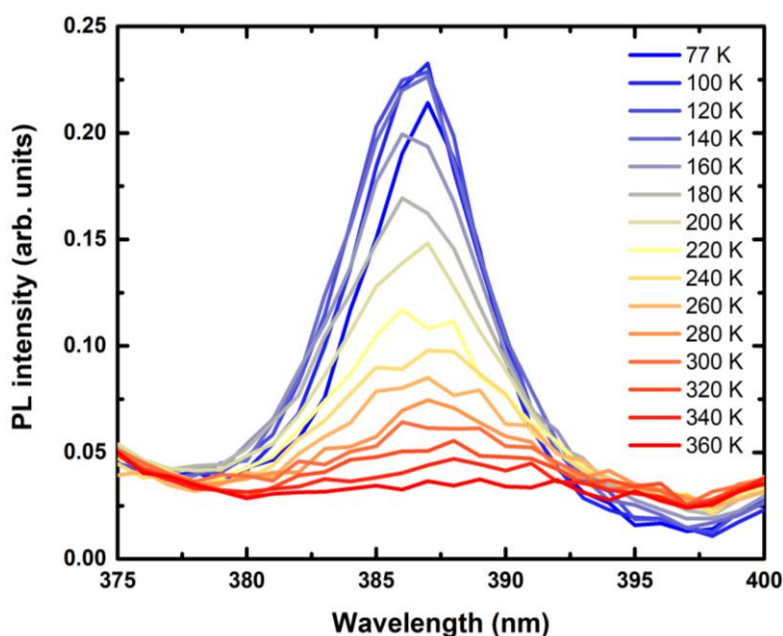


Figure S8. Detail of the temperature dependent excitonic luminescence in the doped perovskite $\text{NMA}_2\text{PbBr}_4:\text{Mn}(10\%)$. Excitation wavelength $\lambda_{\text{exc}}=365$ nm.

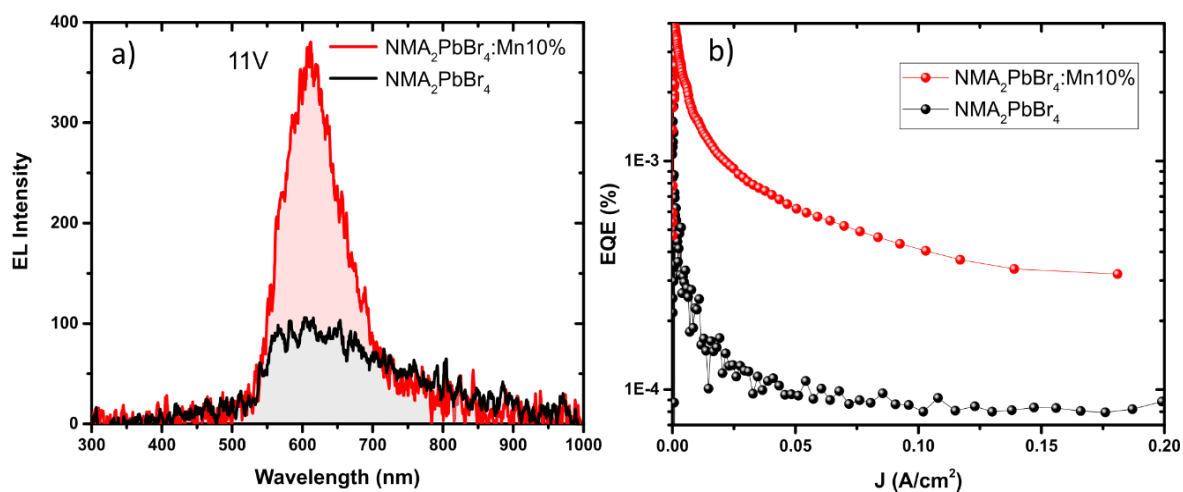


Figure S9. a) Comparison of EL spectra of the non-doped (black line) and doped (red line) perovskite LED at 11 V. The PeLED with Mn inclusion has more intense and narrower spectrum in comparison to the non-doped one. These properties confirm the different nature of the emissions: while for the doped perovskite it originates from Mn centres, in the case of the non-doped device it originates from the NMA phosphorescence. b) External quantum efficiency (EQE) comparison between the LED employing $\text{NMA}_2\text{PbBr}_4$ (black line) and $\text{NMA}_2\text{PbBr}_4:\text{Mn}(10\%)$ (red line) as emitting layer.